

A Multiwavelength Study of the Relativistic Tidal Disruption Candidate *Swift* J2058.4+0516 at Late Times

Dheeraj R. Pasham^{1,2}, S. Bradley Cenko^{1,2}, Andrew J. Levan³, Geoffrey C. Bower⁴, Assaf Horesh⁵, Gregory C. Brown³, Stephen Dolan⁶, Klaas Wiersema⁷, Alexei V. Filippenko⁸, Andrew S. Fruchter⁹, Jochen Greiner¹⁰, Rebekah A. Hounsell⁹, Paul T. O'Brien⁷, Kim L. Page⁷, Arne Rau¹⁰, and Nial R. Tanvir⁷

Email: dheerajrangareddy.pasham@nasa.gov

ABSTRACT

Swift J2058.4+0516 (Sw J2058+05, hereafter) has been suggested as the second member (after Sw J1644+57) of the rare class of tidal disruption events accompanied by relativistic ejecta. Here we report a multiwavelength (X-ray, ultraviolet/optical/infrared, radio) analysis of Sw J2058+05 from 3 months to 3 yr post-discovery in order to study its properties and compare its behavior with that of Sw J1644+57. Our main results are as follows. (1) The long-term X-ray light curve of Sw J2058+05 shows a remarkably similar trend to that of Sw J1644+57. After a prolonged power-law decay, the X-ray flux drops off rapidly by a factor of $\gtrsim 160$ within a span of $\Delta t/t \leq 0.95$. Associating this sudden decline with the transition from super-Eddington to sub-Eddington accretion, we estimate the

¹Code 661, Astrophysics Science Division, NASA's Goddard Space Flight Center, Greenbelt, MD 20771, USA

²Joint Space-Science Institute, University of Maryland, College Park, MD 20742, USA

³Department of Physics, University of Warwick, Coventry, CV4 7AL, UK

⁴Academia Sinica Institute of Astronomy and Astrophysics, 645 N. Aóhoku Place, Hilo, HI 96720, USA

⁵Benoziyo Center for Astrophysics, Faculty of Physics, The Weizmann Institute of Science, Rehovot 76100, Israel

⁶Oxford Astrophysics, Denys Wilkinson Building, Keble Road, Oxford, OX1 3RH, UK

⁷Department of Physics and Astronomy, University of Leicester, University Road, Leicester, LE1 7RH, UK

⁸Department of Astronomy, University of California, Berkeley, CA 94720-3411, USA

⁹Space Telescope Science Institute, 3700 San Martin Drive, Baltimore, MD 21218, USA

¹⁰Max-Planck-Institut für Extraterrestrische Physik, Giessenbachstraße 1, D-85748, Garching, Germany

black hole mass to be in the range of $10^{4-6} M_{\odot}$. (2) We detect rapid ($\lesssim 500$ s) X-ray variability before the dropoff, suggesting that, even at late times, the X-rays originate from close to the black hole (ruling out a forward-shock origin). (3) We confirm using *HST* and VLBA astrometry that the location of the source coincides with the galaxy’s center to within $\lesssim 400$ pc (in projection). (4) We modeled Sw J2058+05’s ultraviolet/optical/infrared spectral energy distribution with a single-temperature blackbody and find that while the radius remains more or less constant at a value of 63.4 ± 4.5 AU ($\sim 10^{15}$ cm) at all times during the outburst, the blackbody temperature drops significantly from $\sim 30,000$ K at early times to a value of $\sim 15,000$ K at late times (before the X-ray dropoff). Our results strengthen Sw J2058+05’s interpretation as a tidal disruption event similar to Sw J1644+57. For such systems, we suggest the rapid X-ray dropoff as a diagnostic for black hole mass.

Subject headings: Black hole physics – relativistic processes – astrometry – accretion, accretion disks

1. Introduction & Background

When a star orbits close to a massive black hole ($M_{\text{BH}} \gtrsim 10^4 M_{\odot}$) such that its periastron distance is $\lesssim R_*(M_{\text{BH}}/m_*)^{1/3}$ (where R_* and m_* are the radius and the mass of the star, respectively), it will be disrupted and cause what is commonly referred to as a tidal disruption event (Hill 1975; Rees 1988). A fraction (roughly 50%) of the stellar debris escapes while the rest is put in a highly eccentric orbit around the black hole, triggering the accretion process (e.g., Evans & Kochanek 1989; Lodato & Rossi 2011). These events are unique in the sense that they provide a one-time opportunity to study the onset of accretion and the formation of accretion disks and jets, which are currently only poorly understood.

For disrupting black holes with masses $\lesssim 4 \times 10^7 M_{\odot}$, the initial accretion rate can exceed their Eddington limit by a factor of a few tens (e.g., Giannios & Metzger 2011). Numerical studies suggest that such high accretion rates should produce outflows/jets driven by strong radiative pressure forces (e.g., Ohsuga et al. 2005). Although the precise jet launching mechanism is still highly debated (see Tchekhovskoy et al. 2010, and references therein), we know from X-ray and radio observations of black hole binaries and active galactic nuclei that jets and accretion are mutually dependent (e.g., Merloni et al. 2003; Falcke et al. 2004; Plotkin et al. 2012). Therefore, accretion initiated by the tidal disruption of a star is anticipated to be a natural site for producing jets.

Given that the black hole jet directions, are uniformly distributed over the sky, most of the jetted events will be offset from our line of sight owing to collimation. Theoretical studies suggest that off-axis relativistic jets, although initially unobservable because of Doppler beaming, should be detectable after a few years when the ejecta slow down to mildly relativistic speeds (Giannios & Metzger 2011). But recent radio follow-up studies of tidal disruption events (TDEs) spanning 1–22 yr after the initial disruption have detected radio emission from only $\lesssim 17\%$ of the sample (see Tables 1 & 2 of van Velzen et al. 2013), suggesting that maybe only a specific subset of events — those requiring special conditions — produce relativistic jets (Bower et al. 2013; van Velzen et al. 2013).

Swift J164449.3+573451 (Sw J1644+57, hereafter) is the first and the best-studied relativistic TDE (one accompanied by a relativistic outflow; e.g., Levan et al. 2011; Bloom et al. 2011; Burrows et al. 2011; Zauderer et al. 2011, 2013). The main observed properties of this source are as follows. (1) Long-lived ($\Delta t \approx 1$ yr), luminous ($L_{X,\text{iso}} \approx 10^{47}$ erg s $^{-1}$), rapidly variable X-ray emission with a power-law secular decline; (2) self-absorbed radio emission indicative of relativistic ejecta; (3) location consistent with the nucleus of a redshift $z = 0.354$, compact, mildly star-forming galaxy; and (4) significant ($\sim 7\%$) near-infrared (NIR) polarization, strongly favoring an on-axis viewing angle (Wiersema et al. 2012). Observations at late times ($\gtrsim 100$ d) have both reinforced and complicated this picture.

The overall trend of Sw J1644+57’s X-ray light curve, neglecting the short-timescale variability, can be described by a more or less constant plateau stage in the first 10 d (rest frame)¹ followed by a power-law decline with an index consistent with both $-5/3$ and -2.2 , corresponding to a complete and a partial disruption of the star², respectively (see Figure 1 of Tchekhovskoy et al. 2014; see also the gray data points in the top panel of Figure 1 of this paper). The X-ray intensity of the source drops abruptly by a factor of ~ 170 over a timescale of $\Delta t/t \lesssim 0.2$ roughly a year after the disruption (see Figure 4 of Zauderer et al. 2013). This has been attributed to jet turnoff when the mass accretion rate dropped below the Eddington value, $\dot{M}_{\text{Edd}} = L_{\text{Edd}}/\eta c^2$, where L_{Edd} , η , and c are the Eddington luminosity, radiative efficiency, and speed of light, respectively (Zauderer et al. 2013).

Radio emission was detected from the source ~ 0.9 d (rest frame) after its discovery in the hard X-rays (Zauderer et al. 2011). This early stage radio emission has been argued

¹All of the durations quoted in this paper will be accompanied by a qualifier indicating whether they were calculated in the rest frame or the observer frame. For instances where a qualifier is not given, it should be assumed that the values are in the observer frame.

²The disruption is partial if the mass lost by the star is $\lesssim 50\%$, while it is referred to as complete if the star loses more than 50% of its mass (Guillochon & Ramirez-Ruiz 2013).

to represent relativistic jetted emission directly pointed along our line of sight (Zauderer et al. 2011). A follow-up radio campaign showed that the radio emission brightened starting about one month after discovery (observer frame; Berger et al. 2012). Berger et al. (2012) interpret this increase in energy as slower ejecta catching up with the forward shock at late times, although other explanations also exist (e.g., Barniol Duran & Piran 2013).

Sw J1644+57 is an exceptional TDE with signatures of a strong jet. Unfortunately, its host galaxy has a large line-of-sight extinction (Levan et al. 2011), making it challenging to study the evolution of the accretion disk expected to be observable in the ultraviolet/optical/infrared (UVOIR; e.g., Strubbe & Quataert 2009; Lodato & Rossi 2011).

Although we have learned a great deal from Sw J1644+57, the question of what aspect makes it conducive to produce a relativistic jet still remains. To answer this question, one approach would be to build a census of Sw J1644+57-like sources. It has also been suggested that Sw J1644+57 could represent a tidal disruption of a white dwarf by a member of the long-sought intermediate-mass black holes (IMBHs; mass range of a few $\times 10^{2-5} M_{\odot}$; Krolik & Piran 2011). With only a handful of strong cases of such black holes known thus far (e.g., ESO HLX X-1: Farrell et al. 2009; Webb et al. 2012; M82 X-1: Kaaret et al. 2009; Pasham, Strohmayer, & Mushotzky 2014), studying such systems could provide insight into weighing and hence identifying such unique objects.

Soon after the 2011 March 25 discovery of Sw J1644+57, *Swift* discovered another transient, *Swift* J2058.4+0516 (hereafter Sw J2058+05), on 2011 May 17 (Cenko et al. 2012; hereafter C12). An early-time ($\lesssim 2$ months since discovery), multiwavelength study showed a number of similarities with Sw J1644+57 (C12). More specifically, Sw J2058+05 occupied the same location in the X-ray versus optical luminosity plot as Sw J1644+57, and its early-phase (20 d after outburst; rest frame) radio, UVOIR, and X-ray spectral energy distribution (SED) was similar to that of Sw J1644+57 (see Figures 4 & 5 of C12). More importantly, strong radio emission coincident with the X-rays was detected ~ 20 d after the initial trigger, suggesting relativistic ejecta (C12). Unlike Sw J1644+57, Sw J2058+05 shows no evidence for line-of-sight extinction (C12), so we can study the system at UVOIR wavelengths in more detail. If it can be established that Sw J2058+05 behaves analogously to Sw J1644+57, then we can start to gain confidence that there is a class of such relativistic TDEs. This paper is a follow-up work to C12 and we address the remaining questions. (1) How does Sw J2058+05 evolve on longer timescales? (2) Assuming the UVOIR can be modeled with a single-temperature blackbody, how do the properties of the putative blackbody evolve on these timescales? (3) Is the emission consistent with originating from the center of the host galaxy? (4) What is the mass of the disrupting black hole?

The paper is arranged as follows. In §2, we discuss the details of our X-ray, UVOIR,

and radio observations. The results and the analysis are described in §3, while we discuss the similarity between Sw J2058+05 and Sw J1644+57, estimate the black hole mass, and so on in §4. We give the main conclusions of this study in §5. Throughout this paper, we adopt a standard Λ CDM cosmology with $H_0 = 71 \text{ km s}^{-1} \text{ Mpc}^{-1}$, $\Omega_m = 0.27$ and $\Omega_\Lambda = 1 - \Omega_m = 0.73$ (Spergel et al. 2007).

2. Data Primer

2.1. X-ray Data

The X-ray data of Sw J2058+05 used in this study were acquired with three different instruments: the X-Ray Telescope (XRT; Burrows et al. 2005) on the *Swift* Gamma-Ray Burst Explorer (Gehrels et al. 2004), the European Photon Imaging Camera (EPIC; Strüder et al. 2001; Turner et al. 2001) on the *XMM-Newton* Observatory (Jansen et al. 2001), and the Advanced CCD Imaging Spectrometer (ACIS; Garmire et al. 2003) on the *Chandra* X-ray observatory (Weisskopf et al. 2002). We describe the data from each of these facilities below.

2.1.1. *Swift*/XRT Observations

Sw J2058+05 was discovered by the BAT (Barthelmy et al. 2005) onboard *Swift* on 2011 May 17 (Krimm et al. 2011). Soon after the BAT detection, starting 2011 May 27, a Target of Opportunity (ToO) program was initiated to monitor this source. Between 2011 May 27 and 2012 July 19 (a temporal baseline of 419 d), *Swift* observed the source on 32 occasions for about 2–3 ks per observation. The data from the first 60 d of this monitoring program have already been reported by C12. They find that the source’s hard X-ray flux falls below the BAT detection limits soon after reaching its peak luminosity (see the top panel of Figure 1 of C12). Here we extended the analysis to late times and use only the XRT X-ray (0.3–10 keV) data from *Swift*.

We started our data analysis with the raw, level-1 XRT data products. Using the latest HEASARC calibration database (CALDB version 20140709) files, we ran *xrtpipeline* to extract the level-2 (scientific) event files. As suggested by the XRT data-analysis guide³, we extracted the exposure maps to take into account the bad pixels and columns (*xrtpipeline*

³ See <http://www.swift.ac.uk/analysis/xrt/lccorr.php>.

with the qualifier *createexpomap=yes*). These exposure maps were then used to correct the ancillary response files (arfs: effective area, using *xrtmkarf*) of each of the 32 observations.

Twenty two of the monitoring observations were taken in the photon-counting (PC) mode, with the remainder in the windowed-timing (WT) mode (see Table 1 for more details). As recommended by the XRT user guide, we only used events with grades 0–12 in the case of PC-mode observations and grades 0–2 for WT-mode data. We then used *XSELECT* to extract energy spectra from each of the individual observations. For the PC-mode data we extracted the source spectra from a circular region centered on J2000.0 coordinates $\alpha = 20^{\text{h}}58^{\text{m}}19.90^{\text{s}}$ and $\delta = +05^{\circ}13'32''.0$, as derived by C12 using the *Chandra*/High-Resolution Camera (HRC) data. We chose an extraction radius of $47''.1$ to include roughly 90% (at 1.5 keV) of the light from the source (as estimated from XRT’s fractional encircled energy function). A background region free of point sources was extracted from a nearby area. Given the low count rates, we chose a radius twice that of the source region in order to better estimate the background. For the WT-mode source region we chose a square box of width $94''.3$ and oriented along the roll angle of the spacecraft — that is, parallel to the WT-mode readout streak. Background was estimated from two square regions (width = $94''.3$) on either side of the source region. The orientation of the square regions (both the source and the background) was adjusted between individual observations to align with the roll angle of the spacecraft during that particular exposure.

2.1.2. *XMM-Newton* Observations

XMM-Newton observed Sw J2058+05 on three occasions (177, 179 and 340 d after the BAT detection; see Table 1 for further details). For the current study, we only used data acquired by EPIC, and both the “pn” and MOS data were used to achieve a higher signal-to-noise ratio (SNR). We started our analysis with the raw observation data files (ODF) and reprocessed them using *XMM-Newton*’s Standard Analysis System’s (SAS) tools *eproc* and *emproc* for the pn and the MOS data, respectively. The standard data filters of (*PATTERN* ≤ 4) and (*PATTERN* ≤ 12) were used for the pn and the MOS data, respectively, and we only considered events in the energy range 0.3–10.0 keV. All the time intervals of prominent background flaring were excluded from the analysis. The source events were extracted from a circular region of radius $33''$. This choice was made to include roughly 90% of the light from the source as estimated from the fractional encircled energy of the EPIC instruments. A background region of similar radius was chosen from a nearby uncontaminated region.

2.1.3. *Chandra/ACIS Observations*

Chandra observed Sw J2058+05 on four occasions. One of the observations was during the early phase of the outburst (C12), while the others were carried out on days 685, 896, and 899 after the initial BAT detection. Since we are interested in the late-time properties of the source, we only utilized the last three observations taken with ACIS. More details about these observations can be found in Table 1. Similar to the XRT and the EPIC data, we started our analysis with level-1 (secondary) data and reprocessed them using *Chandra*'s data-analysis system (CIAO) task *chandra_repro* to account for any calibration changes that may have occurred since the epochs of these observations. Standard data filters were used for reprocessing. All further analysis was carried out on these level-2 event files.

2.2. Ground-Based Optical Photometry Data

Soon after discovery, we started a campaign to carry out multiband photometry of Sw J2058+05 in the UV, optical, and NIR wavebands using multiple instruments. These include the High Acuity Wide field K-band-Imager (HAWK-I; Pirard et al. 2004) and the FOcal Reducer and Spectrograph 2 (FORS2; Appenzeller et al. 1998) on the 8.2 m Very Large Telescope (VLT), and the Gemini Multi-Object Spectrograph (GMOS; Hook et al. 2004) mounted on the 8 m Gemini-South telescope. VLT data were reduced via the standard instrument pipelines for FORS and HAWK-I in *esorex*, while Gemini data were processed using the *gemini IRAF*⁴ package. Photometric calibration was performed relative to nearby point sources from SDSS (optical) and 2MASS (NIR). The resulting photometry, all in the AB magnitude system, is presented in Table 2. The reported magnitudes are not corrected for foreground Galactic extinction along the line of sight to Sw J2058+05 [$E(B - V) = 0.095$ mag; Schlafly & Finkbeiner 2011], but such corrections were applied before all subsequent analysis. The observations prior to 2011 August 12 can be found in Table 1 of C12.

2.3. HST Observations

We observed the location of Sw J2058+05 with the Wide Field Camera 3 (WFC3) on the *Hubble Space Telescope* (*HST*) in three separate epochs: 2011 Aug. 30, 2011 Nov.

⁴IRAF is distributed by the National Optical Astronomy Observatory, which is operated by the Association of Universities for Research in Astronomy (AURA) under a cooperative agreement with the National Science Foundation (NSF).

30 (Proposal GO-12686; PI Cenko) and 2013 Dec. 10 (Proposal GO-13479; PI Levan). Observations were obtained with the $F160W$ filter through the IR channel in all three epochs, as well as with the $F475W$ filter through the UVIS channel in the first two epochs. An additional epoch of imaging was obtained on 2014 Aug. 31 in the $F606W$ filter with the Wide Field Camera (WFC) detector on the Advanced Camera for Surveys (ACS). These data were downloaded after on-the-fly processing from the *HST* archive, and subsequently drizzled using *astrodrizzle* (Fruchter & Hook 2002) to final pixel scales of 65 mas ($F160W$), 30 mas ($F475W$), and 33 mas ($F606W$). We performed aperture photometry at the location of Sw J2058+05 in all images using the prescriptions from the various *HST* handbooks. The resulting photometry, all corrected to the AB system, is displayed in Table 2.

2.4. Optical and Near-Infrared Spectra

We obtained optical and NIR spectra of Sw J2058+05 with the Low-Resolution Imaging Spectrometer (LRIS; Oke et al. 1995) on the 10 m Keck I telescope, FORS2 on the 8 m VLT UT1 (Antu), and the XSHOOTER (Vernet et al. 2011) spectrograph on the 8 m VLT UT2. Details of the configuration for each spectrum are provided in Table 3. For the Keck/LRIS and FORS2 data, one-dimensional spectra were optimally extracted, a wavelength solution was generated from observations of lamps, and flux calibration was performed via spectrophotometric standards. The XSHOOTER spectra were processed through the *reflex* environment. For all spectra the slit was oriented at the parallactic angle to minimize losses caused by atmospheric dispersion (Filippenko 1982).

2.5. Radio Data

We obtained a single epoch of imaging of Sw J2058+05 with the National Radio Astronomy Observatory’s (NRAO⁵) Very Long Baseline Array (VLBA) to search for spatially extended radio emission (project code BC0199). Observations were obtained on 2011 Aug. 12 ($\Delta t \approx 40$ d after discovery, in the rest frame) at central frequencies of 8.4 and 22 GHz with a recording rate of 512 Mb s^{-1} . All 10 stations (SC, HN, NL, FD, LA, PT, KP, OV, BR, and MK) were planned for both frequencies; however, the NL station was lost for our 8 GHz observation (owing to a receiver problem).

⁵The National Radio Astronomy Observatory is a facility of the NSF operated under cooperative agreement by Associated Universities, Inc.

Initial data processing was performed using the AIPS software package (Greisen 2003). J2101+0341 was used for primary phase and astrometric calibration, while J2050+0407 and J2106+0231 were used as secondary calibrators and for evaluation and correction of tropospheric effects on astrometry. The resulting images achieved an angular resolution of ~ 1 mas at 8.4 GHz and 0.3 mas at 22 GHz.

A faint ($f_\nu = 350 \pm 70 \mu\text{Jy}$), unresolved source is detected in the 8.4 GHz image at the J2000.0 position $\alpha = 20^{\text{h}}58^{\text{m}}19.897282^{\text{s}} \pm 0.000006^{\text{s}}$, $\delta = +05^\circ 13' 32''.24306 \pm 0.00016''$ ⁶. No emission is detected at this location in the 22 GHz image to a 3σ upper limit of $f_\nu < 580 \mu\text{Jy}$. Both measurements suggest a decline in radio luminosity by a factor of a few from VLA observations of Sw J2058+05 presented by C12 (~ 20 d rest frame).

3. Analysis

This section is divided into five parts: (1) we show the long-term X-ray light curve of Sw J2058+05 and compare its behavior with that of Sw J1644+57; (2) we carry out astrometry using *HST* and VLBA to pin down Sw J2058+05’s location within its host galaxy; (3) we study the evolution of the UVOIR SED; (4) we analyze the late-time optical spectra; and (5) we consider limits on the size of the radio-emitting region.

3.1. Long-term and Short-term X-ray Light Curves

The individual *Swift*/XRT observations do not have enough counts to constrain the source’s spectral parameters. Hence, we extracted an average energy spectrum by combining all of the XRT PC-mode data⁷. This was achieved by first extracting a source spectrum and a background energy spectrum from each of the 22 observations (most of these observations were at epochs 25–86 d after discovery; rest frame) and then combining them all using the ftool *sumpha*. Similarly, we combined all of the individual ancillary response files, weighted by total counts per observation, using the ftool *addarf*. The response files (RMF) were averaged using the ftool *addrmf*. The combined spectrum was then rebinned using the *grppha* tool to have a minimum of 25 counts per spectral bin.

⁶The reported uncertainties in both RA and DEC are the statistical errors obtained from fits to VLBA data

⁷We excluded the WT-mode data to avoid any systematics caused by the low-energy spectral residuals as described in *Swift* XRT digest at http://www.swift.ac.uk/analysis/xrt/digest_cal.php.

With the latest version of the X-ray spectral fitting package *XSPECv12.8.2* (Arnaud 1996), we then fitted this combined 0.3–10 keV energy spectrum with a power-law model modified by absorption (*phabs*zwabs*pow* in XSPEC). The Galactic column density was fixed at $0.088 \times 10^{22} \text{ cm}^{-2}$ (Kalberla et al. 2005; Willingale et al. 2013)⁸, while the power-law index and the intrinsic absorption column at $z = 1.1853$ (C12) were free to vary. The best-fit power-law index and intrinsic absorption column density were $\Gamma = 1.47 \pm 0.08$ and $n_{\text{H}} = (0.30 \pm 0.15) \times 10^{22} \text{ atoms cm}^{-2}$, respectively (with a reduced $\chi^2 = 0.74$ for 102 degrees of freedom).

We then used these best-fit power-law model parameters (fixing the power-law index and the absorbing column density but keeping the power-law normalization free) and extracted the source flux from each of the individual observations. We only considered observations with a total number of counts greater than 50. In cases where the total number of counts was less than 50, we averaged neighboring observations. The best-fit absorbed power-law model (with fixed power-law index and absorbing column) yielded a reduced χ^2 in an acceptable range of 0.5–1.3 for these individual epochs.

We then fitted each of the three *XMM-Newton*/EPIC (both pn and MOS simultaneously) X-ray spectra of Sw J2058+05 using the same model as above (*phabs*zwabs*pow*). We generated the EPIC response files using the *arfgen* and *rmfgen* tools which are part of *XMM-Newton*'s SAS software. Given that each of these observations had total counts in excess of 1600, we left all the model parameters free to vary except for the redshift and the Milky Way column density. The best-fit model parameters are indicated in Table 4. It is interesting to note that while the best-fit absorbing column densities are consistent with the value derived from the combined *Swift* XRT data acquired at early times, the power-law indices are slightly steeper at late times. The luminosity values derived from modeling the *XMM-Newton* spectra are indicated by the magenta squares in Figure 1.

The source was not detectable in the *Chandra*/*ACIS* images with the naked eye. Nevertheless, using the CIAO task *srcflux*, we estimated an upper limit to the 0.3–10 keV X-ray flux for Poisson statistics. In doing so, we assumed that the source spectrum is defined by an absorbed power-law model with the parameters estimated from the *XMM-Newton* data (see Table 4). The power-law index and the intrinsic absorption column density were set to 1.79 and $0.19 \times 10^{22} \text{ atoms cm}^{-2}$, respectively (mean of the *XMM-Newton* values). The isotropic luminosity upper limits are indicated by the blue squares in Figure 1.

In addition, we studied the short-term variability of the source on timescales of a few hundred to a few thousand seconds using the *XMM-Newton* data. We first extracted a

⁸See <http://www.swift.ac.uk/analysis/nhtot/index.php>.

combined EPIC (pn and MOS) light curve from each of the three *XMM-Newton* observations. One such light curve (black) along with the background (red) binned with a time resolution of 500 s is shown in Figure 2. It is clear that the source varies significantly, with the most drastic variation around 32,000 s when the overall count rate changes by a factor of 2.5 within a timescale of $\lesssim 1000$ s. To further confirm the variability, we modeled the light curve with a constant. The best-fit model gave 0.073 counts s⁻¹ with a reduced χ^2 of 2.3 ($\chi^2 = 236$ for 102 degrees of freedom). Again, this suggests that a constant count rate model is strongly disfavored. Rapid X-ray variability on similar timescales has also been observed from Sw J1644+57 (e.g., Krolik & Piran 2011) and also nonrelativistic TDE candidates such as SDSS J120136.02+300305.5 (see Figure 5 of Saxton et al. 2012).

Finally, to test for any possible coherent oscillations in the X-rays (0.3–10 keV), we extracted a power-density spectrum using the longest *XMM-Newton* observation (ObsID: 0694830201) with an effective exposure of roughly 48 ks. We find that the power spectrum is flat (white noise) and is consistent with being featureless (see Figure 3).

3.2. HST Astrometry

Dynamical friction within a galaxy ensures that supermassive black holes sink to the center within a few Gyr after formation (e.g., Equation 4 of Miller & Colbert 2004). Therefore, if Sw J2058+05 is an event caused by a supermassive black hole, it should arise from the center of the host galaxy. To constrain the (projected) offset between the transient emission from Sw J2058+05 and its underlying host, we took three approaches.

First, we compared the VLBA position for Sw J2058+05 (§2.5) with the host localization derived from *HST*. We used the *F606W* image from 2014 for this purpose (as opposed to the *F160W* images obtained in Dec. 2013), owing to its higher SNR and smaller native pixel scale. While the VLBA position for Sw J2058+05 is the most precise available, the dominant source of uncertainty results from alignment of the *HST* images onto the FK5 reference grid using common point sources from 2MASS (60 mas in each coordinate). After alignment, we measured a position for the host centroid in the *HST* images of $\alpha = 20^{\text{h}}58^{\text{m}}19.898^{\text{s}}$, $\delta = +05^{\circ}13'32''.30$. As this is offset from the VLBA position by 58 mas, we conclude that the radio position is consistent with the host nucleus, within our uncertainties.

Next, we performed digital image subtraction on our *F160W* images obtained on 2011 Aug. 30 (top-left panel of Figure 4) and 2013 Dec. 10 (top-right panel of Figure 4) to more precisely constrain the *relative* transient-host offset (e.g., Levan et al. 2011). The resulting subtraction image is displayed in the bottom-left panel of Figure 4. Assuming that the flux

in the final epoch of imaging is dominated by the host galaxy, we measured a radial offset between the transient emission and the host centroid of 0.34 pixels (i.e., 22 mas). Including contributions to the relative astrometric uncertainty from image alignment (0.18 pixel in each coordinate) and measurement of the host centroid (0.10 pixel in each coordinate), we find a null probability of measuring such an offset of 27% (assuming a Rayleigh distribution for the radial offset). Thus, we conclude that the transient emission is consistent with the host nucleus at this level of precision, as well.

Finally, we measured the relative offset between the 2011 *F475W* images of Sw J2058+05 (dominated by transient emission) and our 2014 *F606W* image of the field (presumed to be host dominated). We find that the centroids in the two images are offset by 10 mas, while our alignment uncertainty is only 15 mas in each coordinate. This method offers the most precise constraint on the relative transient-host offset, and we formally place a 90% confidence limit of $\Delta\theta \lesssim 45$ mas, corresponding to a projected distance of $\lesssim 400$ pc at $z = 1.1853$. This is comparable to the limits on the transient-host offset derived for Sw J1644+57 ($d < 150$ pc (1σ) at $z = 0.354$; Levan et al. 2011).

3.3. Temperature and Radius Evolution of the Blackbody

The UVOIR SED of Sw J2058+05 at early times ($\Delta t \lesssim 1$ yr, observer frame) is quite blue, significantly more so than one would expect from simple forward-shock models (e.g., Granot & Sari 2002). Motivated by the observed SEDs in nonrelativistic TDEs (e.g., Gezari et al. 2012), we fit, wherever possible, the UVOIR SEDs with a single-temperature blackbody. The best-fit model parameters from the six epochs are indicated in Table 5. Including host-galaxy extinction as an additional free parameter in modeling these SEDs did not improve the fits. Formally, we limit the host extinction to $A_V \lesssim 0.2$ mag (90% confidence), assuming it has an extinction law similar to that in the Milky Way (Pei 1992).

All of the SEDs along with the best-fit model are shown in the top panel of Figure 5. We show the evolution of the temperature and the radius of the blackbody in the bottom-left and bottom-right panels, respectively. There is clear evidence for a decrease in the blackbody temperature at late times before the X-ray flux drops off, and marginal evidence for an increase in the radius. But given the large error bars in the radii, we cannot strongly rule-out the possibility that the radius remains constant throughout. We also note, however, that with reduced χ^2 values as low as we find in several epochs, the quoted uncertainties should be treated with some degree of caution. Regardless, it is clear that the emission has become much redder in our final epoch, with a largely flat SED in νL_ν .

3.4. Optical/Near-Infrared Spectra

Our highest-SNR spectrum, obtained with Keck/LRIS on 2011 Aug. 28, is plotted in Figure 6. We also fit our Keck/LRIS spectra to single-temperature blackbody models, and find $T_{\text{BB}} = (1.8 \pm 0.2) \times 10^4 \text{ K}$ on 2011 Aug. 2 and $T_{\text{BB}} = (2.3 \pm 0.1) \times 10^4 \text{ K}$ on 2011 Aug. 28 (solid green line in Figure 6). These results are largely consistent with the values derived from our broadband photometry, providing additional confidence in the above analysis.

For comparison, in Figure 6 we also plot the composite quasar (QSO) spectrum from SDSS (Vanden Berk et al. 2001), and a spectrum taken near maximum light of the TDE PS1-10jh (Gezari et al. 2012). In all cases the spectra of Sw J2058+05 are dominated by a blue, featureless continuum. No obvious emission or absorption features are detected in any spectra, with the exception of the initial spectrum from 2011 June 1 presented in C12, from which the redshift of $z = 1.1853$ was derived from narrow Mg II and Fe II absorption lines. Clearly, the strong, broad emission lines that dominate QSOs in the near-UV (e.g., Mg II, C III], and C IV) are not present in our spectra of Sw J2058+05. In addition to a hot ($T_{\text{BB}} \approx 3 \times 10^4 \text{ K}$) blackbody continuum, PS1-10jh displayed high-ionization He II $\lambda 4686$ and $\lambda 3203$ emission lines. Our Keck/LRIS spectra do not probe sufficiently far into the rest-frame optical to cover the stronger He II $\lambda 4686$ feature. We see no evidence for broad emission at this location in our XSHOOTER spectra; however, the SNR is quite low in these data. A number of optically discovered TDEs also display broad $\text{H}\alpha$ emission (Arcavi et al. 2014; Holoien et al. 2014), although it is unclear if the presence/absence of H is due to properties of the disrupted star (Gezari et al. 2012) or the radial extent of the newly formed accretion disk (Guillochon et al. 2014). Again, we detect no evidence for broad emission lines at rest-frame $\text{H}\alpha$ (or any other Balmer lines, for that matter), but are limited by the low SNR at these wavelengths.

We can also limit the presence of narrow, nebular emission lines from the underlying host galaxy. In particular, we do not detect either [O II] $\lambda 3727$ or $\text{H}\alpha$. If we assume unresolved emission lines at these wavelengths, we calculate limiting flux values of $f(\text{O II}) < 4.8 \times 10^{-17} \text{ erg s}^{-1} \text{ cm}^{-2}$ and $f(\text{H}\alpha) < 6.5 \times 10^{-17} \text{ erg s}^{-1} \text{ cm}^{-2}$. Using the relations from Kennicutt (1998) between emission-line luminosity and star-formation rate, we limit the presence of recent star formation in the host of Sw J2058+05 to be $\lesssim 5 M_{\odot} \text{ yr}^{-1}$ (uncorrected for extinction). This is consistent with an estimate of the star-formation rate derived from the UV ($F606W$) luminosity of the host galaxy, for which we find $0.8 M_{\odot} \text{ yr}^{-1}$ (using the calibration from Kennicutt 1998).

3.5. Size of the Radio-Emitting Region

The detection of radio emission from Sw J2058+05 confirms the presence of nonthermal electrons in the circumnuclear ejecta. We can apply standard equipartition arguments (Readhead 1994; Kulkarni et al. 1998) to place a lower limit on the size of the radio-emitting region. Using the formulation valid for relativistic outflows from Barniol Duran et al. (2013), our VLBA detection at $\Delta t \approx 40$ d (rest frame) implies $R_{\text{eq}} \gtrsim 7 \times 10^{16}$ cm. Similarly, these observations, though not as constraining as those presented by C12⁹, imply at least transrelativistic expansion ($\Gamma_{\text{eq}} \gtrsim 0.6$) from an energetic outflow ($E_{\text{eq}} \gtrsim 3 \times 10^{49}$ erg).

The above limit on the physical size of the radio-emitting region corresponds to a lower limit on the angular size of $\Theta \gtrsim 3\Psi \mu\text{as}$, where Ψ is the jet opening angle. For any feasible jet opening angle, this result is consistent with the unresolved nature of the source in the VLBA imaging ($\Theta \lesssim 1$ mas).

4. Discussion

4.1. Radiation Mechanisms and the Broadband SED

To better understand the nature of Sw J2058+05, we first consider the origin of the emission in the three regimes probed here: radio, UVOIR, and X-ray. We derived a robust lower limit on the size of the radio-emitting region (based solely on equipartition arguments in §3.5), $R_{\text{radio}} \gtrsim 7 \times 10^{16}$ cm. Together with more stringent limits on the bulk Lorentz factor from C12 ($\Gamma \gtrsim 1.5$), we conclude that the radio emission is generated by the forward shock of a newly formed, at least mildly relativistic jet. An identical conclusion was reached by several authors (e.g., Zauderer et al. 2011; Bloom et al. 2011) in the case of Sw J1644+57.

The X-rays, on the other hand, must clearly have a distinct origin. The rapid variability on a rest-frame timescale of $\lesssim 500$ s require the size of the X-ray-emitting region to be $R_{\text{X-ray}} \lesssim c \delta t \approx 2 \times 10^{13}$ cm. This clearly rules out a forward-shock origin. However, the tremendous peak X-ray luminosity, many orders of magnitude above Eddington for any feasible black hole, suggests some association with the newly formed jet (as does the rapid turnoff; see below). One possibility is that the X-rays are generated in the base of the jet (e.g., Bloom et al. 2011; Zauderer et al. 2011), though the process by which this occurs remains a mystery. Again, the analogy with Sw J1644+57 holds well.

⁹Applying the same formulation to the VLA data from C12, we find $R_{\text{eq}} \gtrsim 6 \times 10^{16}$ cm, $\Gamma_{\text{eq}} \gtrsim 1.5$, and $E_{\text{eq}} \gtrsim 4 \times 10^{49}$ erg.

Finally, we have demonstrated that the UVOIR data, both photometry and spectra, are well fit by a single-temperature blackbody with $T_{\text{BB}} \approx \text{few} \times 10^4$ K. The inferred blackbody radius, which appears to remain roughly constant, is $R_{\text{opt}} \approx 10^{15}$ cm. Together with the long-lived blue colors, the radius also seems to disfavor a forward-shock origin for the UVOIR component. Similarly, the derived blackbody spectrum severely underpredicts the observed X-ray flux.

Instead, these values are consistent with spectral studies of nonrelativistic TDE candidates in the literature with apparent blackbody temperatures and radii in the range of $(1\text{--}10) \times 10^4$ K and $(0.1\text{--}20) \times 10^{15}$ cm, respectively (e.g., Gezari et al. 2009b, 2012; Armijo & de Freitas Pacheco 2013; Guillochon et al. 2014; Chornock et al. 2014; Cenko et al. 2012b; Holoien et al. 2014; Arcavi et al. 2014), although there are some TDE candidates that tend to show higher disk temperatures of $\gtrsim 10^5$ K accompanied by smaller emitting regions of size $\lesssim 10^{13}$ cm (e.g., Gezari et al. 2008). However, for any plausible black hole mass, the blackbody radius is orders of magnitude larger than the radius at which disruption should occur. Such large radii have been attributed to reprocessing in some external region (see, for example, the numerical simulations of Guillochon et al. 2014).

It is important to note here, that while Sw J1644+57 lacked detectable UV and optical emission, the high degree of polarization observed in the NIR was attributed to jetted emission from the forward shock (Wiersema et al. 2012), and not from the (presumably largely isotropic) accretion disk. Naively, unless the reprocessing region was nonisotropic, we would expect a low degree of optical polarization from Sw J2058+05 if this simplistic picture is correct. For future relativistic TDE candidates, polarization observations would be an important test of this model.

4.2. Energetics

Using the best-fit blackbody luminosities and integrating the resulting light curve (using the trapezoidal rule) in the rest frame between epochs 5.7 and 181.4 d, we estimate the total UVOIR energy radiated to be $\sim 5 \times 10^{51}$ erg. Similarly, we integrated the X-ray light curve (top panel of Figure 1) and estimate the total isotropic energy to be $\sim 4 \times 10^{53}$ erg. Assuming an opening angle of ~ 0.1 rad, similar to what has been estimated for Sw J1644+57 (Zauderer et al. 2013; Metzger et al. 2012), we measure the total, beaming-corrected X-ray energy output to be $\sim 4 \times 10^{51}$ erg. The bolometric luminosity is, however, expected to be a factor of a few higher than the X-ray luminosity. Assuming the bolometric value is a factor of 3 (similar to that of Sw J1644+57; Burrows et al. 2011), one can estimate the total accreted mass onto the black hole using Equation 5 of the supplemental information of Burrows et al.

(2011). We find this value to be $\sim 0.1 M_{\odot}$, which is comparable to Sw J1644+57’s $0.2 M_{\odot}$ (Burrows et al. 2011; Zauderer et al. 2013), both appropriate for disruption of a $\sim 1 M_{\odot}$ star.

4.3. Nature of the Rapid X-ray Dropoff

The X-ray emission from Sw J2058+05 drops abruptly between days 200 and 300 (rest frame), consistent with what was seen for Sw 1644+57 (top panel of Figure 1). More specifically, Sw J2058+05’s intensity decreases by a factor of $\gtrsim 160$ within a span of $\Delta t/t \leq 0.95$ compared to Sw J1644+57’s factor of ~ 170 decline over a span of $\Delta t/t \lesssim 0.2$ (Levan & Tanvir 2012; Sbarufatti et al. 2012; Zauderer et al. 2013). Interestingly, in both of these sources, the X-ray dimming occurs on a comparable timescale after disruption.

In the case of Sw J1644+57, Zauderer et al. (2013) interpreted this sudden decrease in the flux as an accretion-mode transition from a super-Eddington to a sub-Eddington state. This is consistent with the transitioning timescale predicted from numerical simulations (e.g., Figures 4 & 2 of Evans & Kochanek 1989 and De Colle et al. 2012, respectively). Assuming the same process is responsible for the abrupt flux change in Sw J2058+05, we can attempt to estimate the mass of the black hole by equating the luminosity at turnoff to the Eddington luminosity. From the X-ray light curve (see Tables 1 & 4), it is evident that the isotropic X-ray luminosity drops from $1.3 \times 10^{45} \text{ erg s}^{-1}$ to less than $8.4 \times 10^{42} \text{ erg s}^{-1}$, suggesting an Eddington value somewhere in between these two limits. Using these two values and assuming radiative efficiency, beaming angle, and bolometric correction values of 0.1, 0.1 rad, and 30%, respectively (similar to Sw J1644+57; Burrows et al. 2011), we constrained the black hole mass M_{BH} to be $10^4 M_{\odot} \lesssim M_{\text{BH}} \lesssim 2 \times 10^6 M_{\odot}$. Furthermore, numerical simulations suggest that the time to dropoff (transition from super-Eddington to sub-Eddington) since the disruption is shorter for more massive black holes (see Figure 2 of De Colle et al. 2012). The X-ray dropoff in Sw J2058+05 occurs ~ 100 d earlier than that in Sw J1644+57, suggesting that its black hole may be more massive.

However, it is interesting to note that even the optical light curves of Sw J2058+05 undergo an abrupt change during an epoch roughly consistent with the X-ray dimming (see the bottom panel of Figure 1). We find that the optical flux, for instance in the r band, drops by a factor of at least 5 within a narrow span of $\Delta t/t \approx 0.16$. We speculate, within the context of the following simple model, that the X-rays are coming from the base of the jet and the optical originates from the reprocessed UV/soft-X-ray disk photons in the ambient medium. In such a scenario, the proposed super-Eddington to sub-Eddington accretion transition would presumably change the accretion-disk structure to lower its emission, thus

explaining the reduction in the amount of the reprocessed light. Obviously, the true situation is more complicated, with specific details about the radiative efficiency, beaming, and other factors. It can be better understood with more detailed modeling, but this is beyond the scope of the current paper.

On the other hand, the longterm X-ray light curve of Sw J2058+05 does not exhibit the numerous sudden dips observed in Sw J1644+57 (see Figure 1). In the case of Sw J1644+57, it has been argued that the X-ray dips originate from jet precession and nutation, which causes it to briefly to go out of our line of sight (e.g., Saxton et al. 2012). We speculate, based on the lack of such dips in Sw J2058+05, that its jet may be more stable compared to Sw J1644+57. However given the poor sampling of the X-ray light curve, the current data cannot completely rule-out the presence of dips in Sw J2058+05.

4.4. Other M_{BH} Estimates

The mass limits derived above based on the X-ray turnoff are consistent with other methods of estimating M_{BH} . First, we can use the X-ray variability timescale to place an upper limit on black hole mass. Equating the limit on the size of the X-ray-emitting region with a Schwarzschild radius suggests a compact object of mass less than $5 \times 10^7 M_{\odot}$.

Also, assuming that the optical flux in our final two *HST* epochs is dominated by the host galaxy (and not transient emission), we can constrain the mass of the central supermassive black hole using the well-known bulge luminosity vs. black hole mass relations (e.g., Lauer et al. 2007). Neglecting for the moment K-corrections [aside from the cosmological $-2.5 \log(1+z)$ factor], the distance modulus at $z = 1.1853$ implies an absolute magnitude of -18.7 from the *F606W* observation (approximately rest-frame *U* band) and -19.4 from the *F160W* observation (approximately rest-frame *I* band). Both suggest $M_V \approx -19$ mag, or an inferred supermassive black hole mass of $M_{\text{BH}} \lesssim 3 \times 10^7 M_{\odot}$. While there is significant scatter in the bulge luminosity vs. black hole mass relation, our limits are conservative in the sense that they assume *all* of the observed luminosity derives from the bulge (and none from, say, a disk). At the very least, we can robustly conclude that $M_{\text{BH}} < 10^8 M_{\odot}$, the limit above which a nonspinning black hole cannot tidally disrupt a solar mass main-sequence star (Rees 1988).

5. Conclusions

The goal of this work is to use multiwavelength data and study the long-term (~ 1 yr) behavior of candidate relativistic TDE Sw J2058+05. Our main conclusions are as follows.

(1) The long-term X-ray turnoff and the host-galaxy nuclear association of Sw J2058+05 strengthen the similarity between Sw J2058+05 and Sw J1644+57.

(2) Rapid X-ray variability on a timescale $\lesssim 500$ s at late times (before the X-ray dropoff) suggests that X-ray photons originate near the black hole and not from a forward shock. If the X-rays were to come from the forward shock, they would vary on much longer timescales.

(3) Based on the blackbody modeling of the optical data of Sw J2058+05 (in ways not possible with Sw J1644+57 because of the large host-galaxy extinction), we find that the optical originates from farther out ($\sim 10^{15}$ cm) than the X-rays. Also, the UVOIR SED modeling severely underpredicts the X-ray emission. Lastly, the early-time optical data did not show variability on timescales of a few 1000 s, suggesting again an emission size of larger than a few 1000 light seconds. However, the X-rays originate very close to the black hole. We conclude based on these lines of evidence that the optical and the X-rays have distinct origins.

(4) The size of the optically emitting region of Sw J2058+05 suggests that it originates from reprocessing. The fact that reprocessing is seen in X-ray-selected events (as well as optical ones) suggests it is a relatively common phenomenon.

(5) In Sw J2058+05-like events, the X-ray dropoff (both the flux or the timescale measurements) could be a probe of the black hole mass.

(6) These observations imply the need for improved modeling to better understand Sw J2058+05-like events.

Facilities: Swift (XRT), XMM (EPIC), Chandra (ACIS), VLT (FOR2, HAWK-I, XSHOOTER), Keck (LRIS), Gemini:South (GMOS-S), HST (WFC3, ACS), VLBA

We thank the *XMM-Newton* and *HST* teams, in particular Project Scientist N. Schartel and STScI director M. Mountain, for the approval and prompt scheduling of our DD requests. We are also grateful to James Guillochon and Ryan Chornock for valuable discussions. D.R.P. is grateful for valuable discussions with Sjoert van Velzen and Nick Stone. S.B.C. thanks the Aspen Center for Physics and NSF Grant #1066293 for hospitality during the preparation of this manuscript. K.L.P. acknowledges support from the UK Space Agency. Support for this work was provided by the National Aeronautics and Space Administration (NASA)

through Chandra Award Number GO3-14107X issued by the Chandra X-ray Observatory Center, which is operated by the Smithsonian Astrophysical Observatory for and on behalf of NASA under contract NAS8-03060. D.R.P. and S.B.C. also acknowledge support from *HST* grant GO-13611-006-A. The work of A.V.F. was made possible by NSF grant AST-1211916, the TABASGO Foundation, and the Christopher R. Redlich Fund. A.V.F. and S.B.C. also acknowledge the support of Gary and Cynthia Bengier. Finally, we would like to thank the referee for his/her careful comments and suggestions.

The scientific results reported in this article are based in part on observations made by the *Chandra* X-ray Observatory, NASA/ESA *Hubble Space Telescope*, obtained from the Data Archive at the Space Telescope Science Institute, which is operated by the Association of Universities for Research in Astronomy, Inc., under NASA contract NAS 5-26555 and, *XMM-Newton*, an ESA science mission with instruments and contributions directly funded by ESA Member States and NASA. Some of the data presented herein were obtained at the W. M. Keck Observatory, which is operated as a scientific partnership among the California Institute of Technology, the University of California, and NASA; the observatory was made possible by the generous financial support of the W. M. Keck Foundation. Also, observations were obtained at the Gemini Observatory, which is operated by the Association of Universities for Research in Astronomy, Inc., under a cooperative agreement with the NSF on behalf of the Gemini partnership: the National Science Foundation (United States), the National Research Council (Canada), CONICYT (Chile), the Australian Research Council (Australia), Ministério da Ciência, Tecnologia e Inovação (Brazil) and Ministerio de Ciencia, Tecnología e Innovación Productiva (Argentina). Also, based on observations made with ESO Telescopes at the La Silla or Paranal Observatories. We acknowledge the use of public data from the Swift data archive.

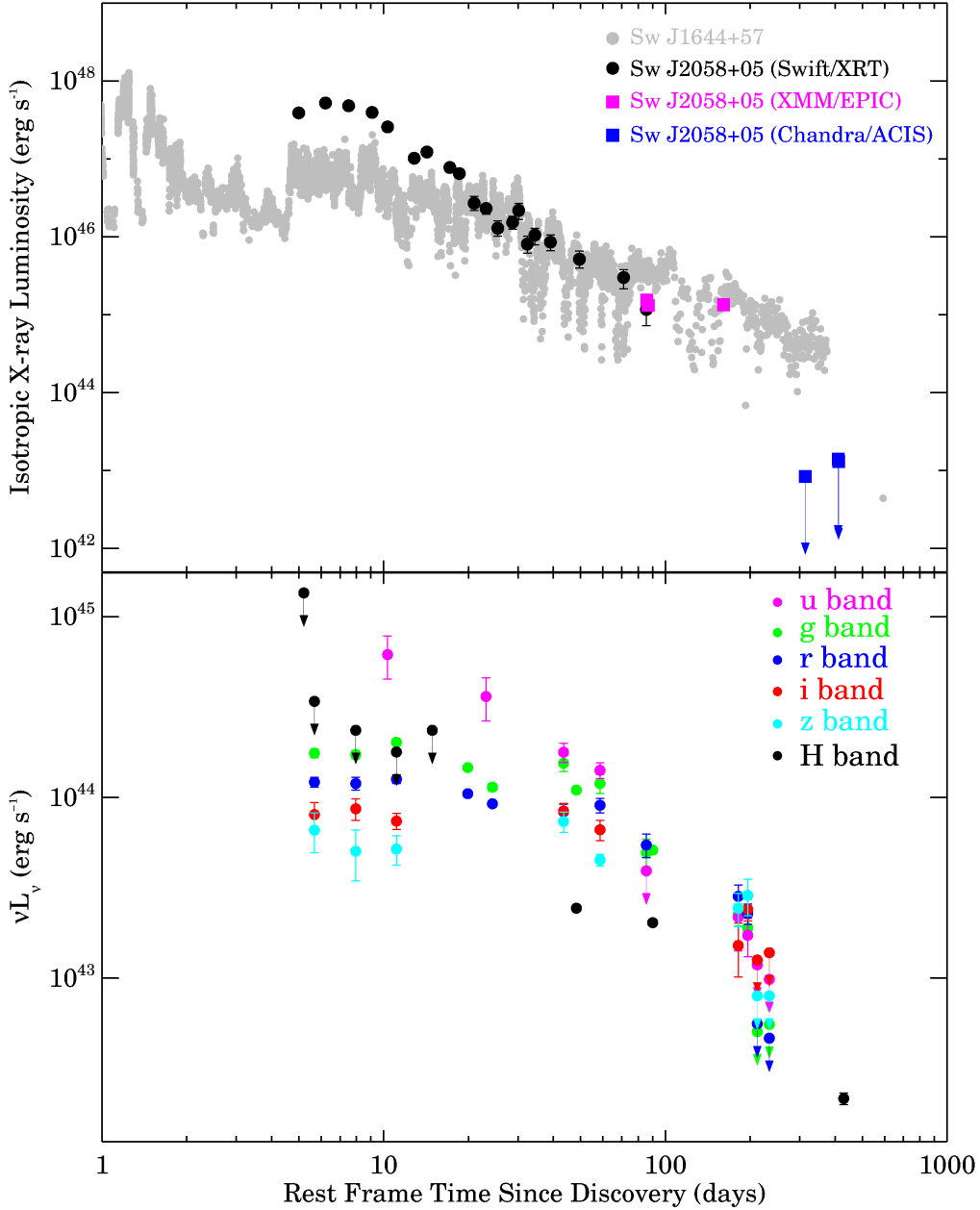


Figure 1: *Top panel:* Comparing the long-term X-ray (0.3–10 keV) light curve of Sw J2058+05 (filled circles and squares) with that of Sw J1644+57 (gray; adapted from Burrows et al. 2011). An abrupt decline in the X-ray luminosity seen in Sw 1644+57 (Zauderer et al. 2013) is also evident in Sw J2058+05. The magenta squares are flux estimates of Sw J2058+05 from *XMM-Newton*/EPIC, while the blue are the upper limits from *Chandra*/ACIS (see Table 1). The discovery time of Sw J2058+05 is not precisely constrained, but we refer to the time of discovery as 00:00:00 on 2011 May 17 (MJD = 55698) as per Cenko et al. (2012). The rest-frame time was thus estimated as $(\text{time} - 55698)/(1 + z)$, where $z = 1.1853$. *Bottom panel:* The long-term light curve of Sw J2058+05 in various optical bands (data available in Table 2), showing a similar sharp decline as seen in the X-rays.

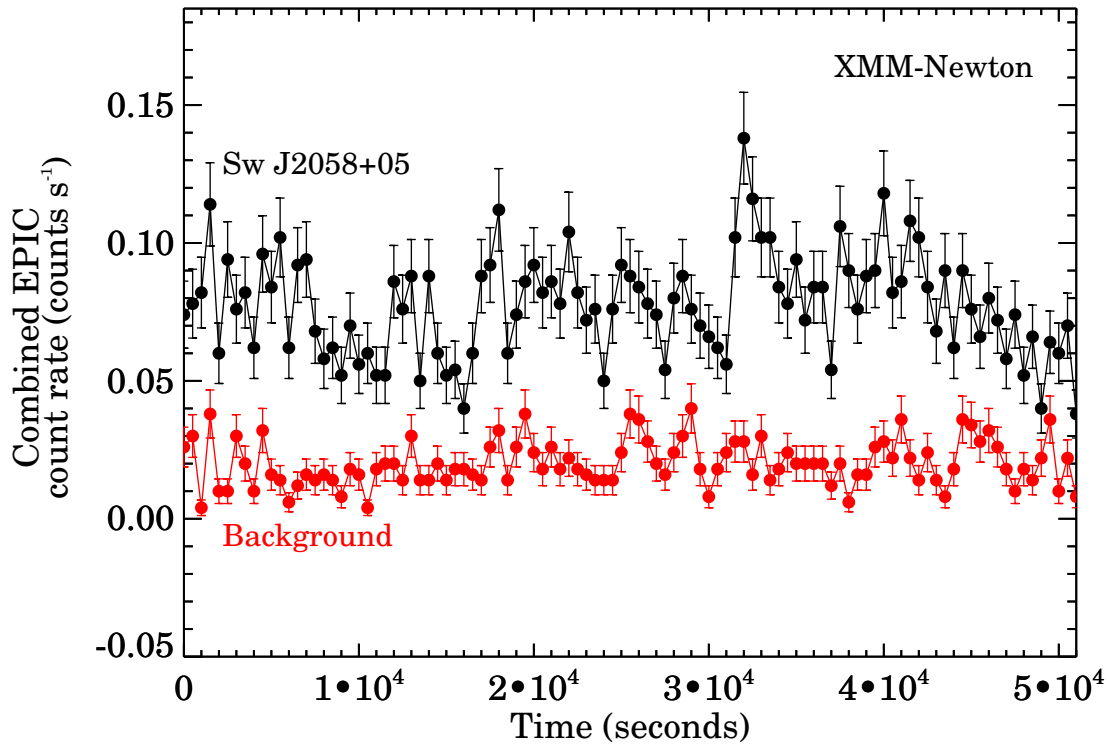


Figure 2: *XMM-Newton*/EPIC (both pn and MOS) X-ray (0.3–10 keV) light curve of Sw J2058+05 (filled black circles), highlighting X-ray variability on timescales of ~ 500 s. The light curve was derived from the longest good time interval of 50 ks from the *XMM-Newton* observation with ID 0694830201 and binned at 500 s. The background during the same time is shown in red. The source light curve was fit to a constant-flux model and shows clear variability ($\chi^2 = 236$ for 102 degrees of freedom).

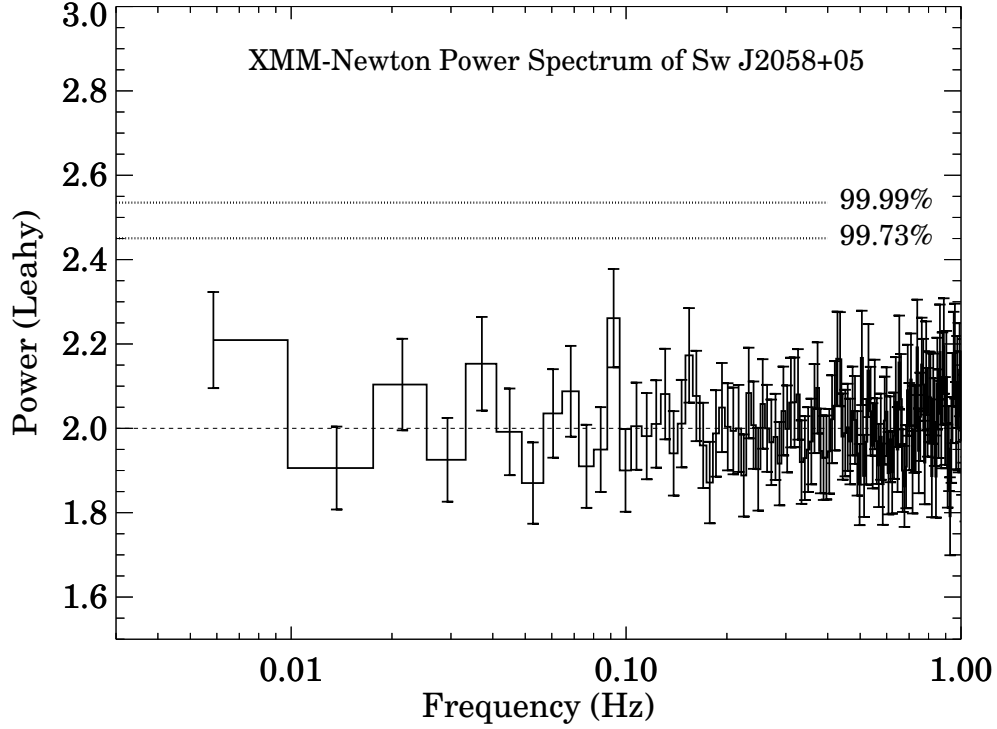


Figure 3: *XMM-Newton*/EPIC-pn (ObsID: 0694830201) X-ray (0.3–10 keV) power density spectrum of Sw J2058+05. The power spectrum is Leahy normalized (Leahy 1983) with a Poisson noise level of 2 (dashed horizontal line). The frequency resolution is 7.8 mHz and each bin is an average of 188 independent power spectral measurements. The confidence limits ($3\sigma/99.73\%$ and $3.9\sigma/99.99\%$) are indicated by the two horizontal dotted lines. The spectrum is featureless and consistent with being flat (white noise).

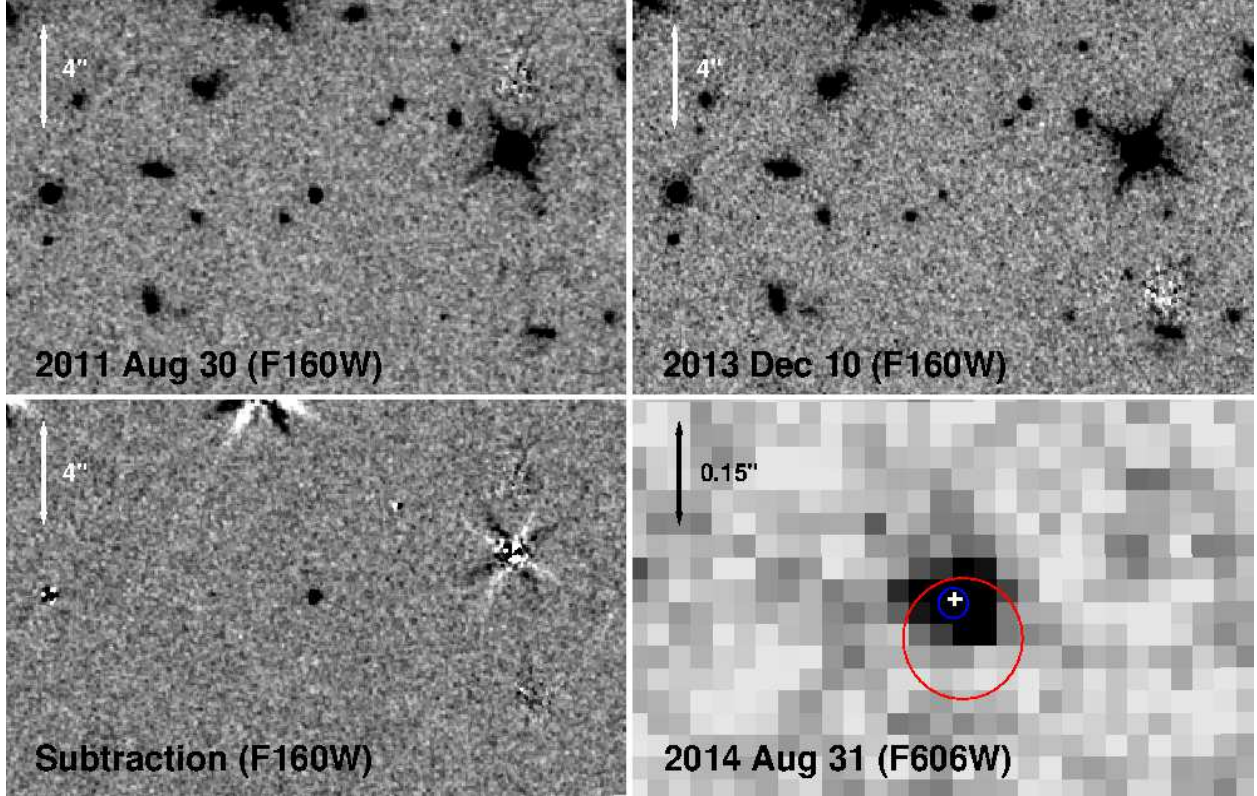


Figure 4: *Top-left panel:* *HST/WFC3 F160W* image of the location of Sw J2058+05 obtained on 2011 Aug. 30 (two months after Sw J2058+05 reached its peak luminosity). *Top-right panel:* An image of Sw J2058+05 with the identical instrument configuration from 2013 Dec. 10 (long after the outburst when the optical emission is dominated by the host galaxy). *Bottom-left panel:* Digital image subtraction of the two *F160W* frames. To within measurement uncertainties, the location of the resulting transient emission is consistent with the centroid of the host galaxy. *Bottom-right panel:* Zoomed-in image of the host galaxy in the *F606W* filter. The centroid of the host galaxy is indicated by the white cross. Our most precise astrometric constraints come from aligning this *F606W* image from 2014 Aug 31 with a previous HST image of the transient from 2011 Aug 30 in the *F475W* filter, for which the 68% confidence uncertainty in the astrometric tie between the two frames is 23 mas in radius (blue circle). The VLBA position for Sw J2058+05, along with the uncertainty in connecting the VLBA position to the HST astrometric frame (68% confidence radius of 90 mas) is indicated by the red circle.

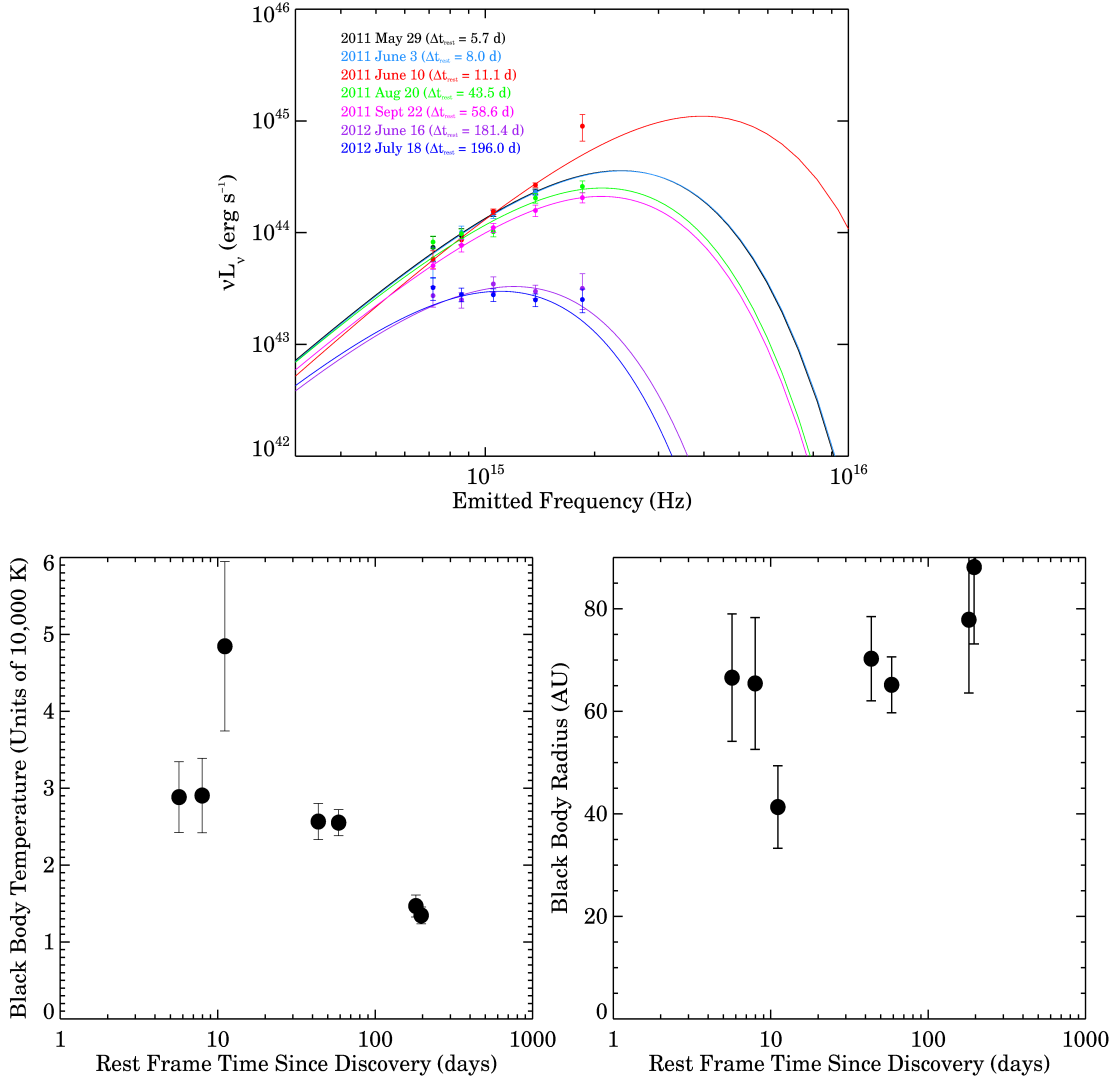


Figure 5: *Top panel:* UVOIR SEDs of Sw J2058+05 at various epochs (filled circles). The best-fit single-temperature blackbodies (solid curves) are also shown. Δt_{rest} refers to days in rest frame since discovery. *Bottom-left panel:* The blackbody temperature as a function of the rest-frame time since discovery. *Bottom-right panel:* The blackbody radius as a function of the rest-frame time since discovery. All of the error bars indicate 90% confidence limits.

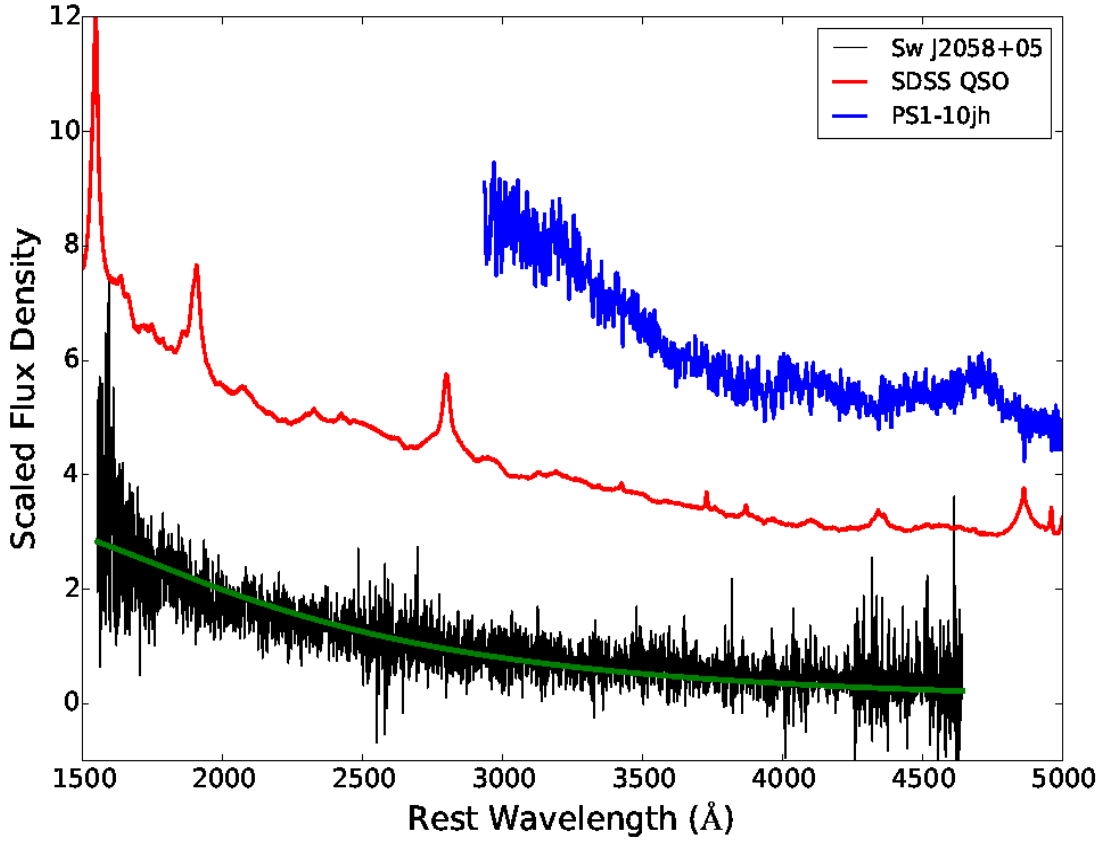


Figure 6: Optical and NIR spectra of Sw J2058+05 (black) taken with Keck/LRIS on 2011 Aug. 28 (~ 47 d after discovery, measured in the rest frame). The solid green line shows a fit to a single blackbody with $T_{\text{BB}} = (2.3 \pm 0.1) \times 10^4$ K. For comparison, the composite SDSS spectrum of quasars (Vanden Berk et al. 2001) and the spectrum of the TDE PS 1-10jh taken at its peak luminosity (Gezari et al. 2012) are shown in red and blue, respectively. The spectrum of Sw J2058+05 does not contain any apparent absorption or emission lines at this stage.

Table 1: Summary of X-ray Spectral Modeling of Sw J2058+05

Instrument	ObsID	MJD Date ^{††}	X-ray Flux [*]	Notes [†]
<i>Swift</i> /XRT	00032004001	55708.915	$48.12^{+1.61}_{-1.70}$	PC Mode
<i>Swift</i> /XRT	00032004002	55711.582	$64.49^{+2.20}_{-2.19}$	WT Mode
<i>Swift</i> /XRT	00032004003	55714.412	$59.37^{+2.24}_{-2.08}$	WT Mode
<i>Swift</i> /XRT	00032004004	55717.879	$48.78^{+1.62}_{-1.51}$	WT Mode
<i>Swift</i> /XRT	00032004005	55720.568	$31.78^{+1.66}_{-1.59}$	WT Mode
<i>Swift</i> /XRT	00032004007	55726.045	$12.61^{+0.90}_{-0.88}$	WT Mode
<i>Swift</i> /XRT	00032004008	55729.110	$15.17^{+1.08}_{-1.02}$	WT Mode
<i>Swift</i> /XRT	00032004009	55735.539	$9.58^{+0.84}_{-0.78}$	WT Mode
<i>Swift</i> /XRT	00032004010	55738.548	$8.01^{+0.79}_{-0.89}$	WT Mode
<i>Swift</i> /XRT	00032026001	55743.760	$3.33^{+0.74}_{-0.64}$	WT Mode
<i>Swift</i> /XRT	00032026002	55748.457	$2.85^{+0.38}_{-0.43}$	WT Mode
<i>Swift</i> /XRT	00032026003	55753.531	$1.59^{+0.38}_{-0.34}$	PC Mode
<i>Swift</i> /XRT	00032026004	55760.699	$1.90^{+0.36}_{-0.34}$	PC Mode
<i>Swift</i> /XRT	00032026005	55763.907	$2.69^{+0.64}_{-0.64}$	PC Mode
<i>Swift</i> /XRT	00032026006	55768.723	$0.99^{+0.25}_{-0.23}$	PC Mode
<i>Swift</i> /XRT	00032026007	55773.203	$1.30^{+0.28}_{-0.32}$	PC Mode
<i>Swift</i> /XRT	00032026009	55783.373	$1.05^{+0.24}_{-0.24}$	PC Mode
<i>Swift</i> /XRT	00032026010-012	55806.229	$0.64^{+0.17}_{-0.15}$	PC Mode
<i>Swift</i> /XRT	00032026013-015	55853.296	$0.37^{+0.09}_{-0.11}$	PC Mode
<i>Swift</i> /XRT	00032026016-021	55885.110	$0.14^{+0.05}_{-0.05}$	PC Mode
<i>XMM-Newton</i> /EPIC	0679380801	55885.635	$0.19^{+0.02}_{-0.02}$	Exposure: 23 ks
<i>XMM-Newton</i> /EPIC	0679380901	55887.787	$0.16^{+0.02}_{-0.02}$	Exposure: 29 ks
<i>XMM-Newton</i> /EPIC	0694830201	56049.048	$0.17^{+0.01}_{-0.01}$	Exposure: 55 ks
<i>Chandra</i> /ACIS	14975	56383.806	$\leq 1.05 \times 10^{-3}$	Exposure: 30 ks
<i>Chandra</i> /ACIS	16498	56594.972	$\leq 1.76 \times 10^{-3}$	Exposure: 20 ks
<i>Chandra</i> /ACIS	14976	56597.639	$\leq 1.63 \times 10^{-3}$	Exposure: 30 ks

^{††}The source was discovered on MJD 55698. ^{*}The X-ray fluxes were estimated in the bandpass of 0.3–10 keV and have units of $10^{-12} \text{ erg s}^{-1} \text{ cm}^{-2}$. These represent the values just outside our Galaxy. The X-ray luminosities in the top panel of Figure 1 were estimated as $\text{flux} \times 4\pi D^2$, where D is 8200 Mpc. See text for details on the modeling. [†]PC refers to photon counting and WT to windowed timing.

Table 2: A Summary of UV/Optical/IR observations of Sw J2058+05

UTC date	MJD Date	Telescope	Filter	Exposure (seconds)	AB Magnitude*
2011 Aug 12.05	55785.05	VLT - HAWK-I	J	1020	22.72 ± 0.33
2011 Aug 12.07	55785.07	VLT - HAWK-I	K	1080	> 21.6
2011 Aug 20.07	55793.07	VLT - FORS 2	u	840.0	22.86 ± 0.13
2011 Aug 20.07	55793.07	VLT - FORS 2	g	120.0	22.69 ± 0.11
2011 Aug 20.07	55793.07	VLT - FORS 2	r	120.0	23.07 ± 0.11
2011 Aug 20.08	55793.08	VLT - FORS 2	i	200.0	22.84 ± 0.11
2011 Aug 20.08	55793.08	VLT - FORS 2	z	720.0	22.79 ± 0.14
2011 Aug 30.56	55803.56	HST - WFC3	F160W (H band) ^{††}	1196.9	23.36 ± 0.02
2011 Aug 30.58	55803.58	HST - WFC3	F475W (SDSS g) [†]	1110.0	23.06 ± 0.02
2011 Sept 2.21	55806.21	VLT - HAWK-I	J	1020	22.22 ± 0.22
2011 Sept 2.21	55806.21	VLT - HAWK-I	K	1080	21.87 ± 0.25
2011 Sept 22.06	55826.06	VLT - FORS 2	r	120.0	22.98 ± 0.10
2011 Sept 22.07	55826.07	VLT - FORS 2	u	840.0	23.11 ± 0.11
2011 Sept 22.07	55826.07	VLT - FORS 2	g	120.0	22.97 ± 0.13
2011 Sept 22.08	55826.07	VLT - FORS 2	i	200.0	23.10 ± 0.14
2011 Sept 22.08	55826.07	VLT - FORS 2	z	720.0	23.32 ± 0.08
2011 Sept 24.99	55828.99	VLT - HAWK-I	J	1020	22.46 ± 0.16
2011 Sept 25.01	55829.01	VLT - HAWK-I	K	1080	21.60 ± 0.20
2011 Nov 20.02	55885.02	Gemini-S - GMOS	u	300.5	> 24.5
2011 Nov 20.02	55885.02	Gemini-S - GMOS	g	100.5	23.93 ± 0.21
2011 Nov 20.03	55885.02	Gemini-S - GMOS	r	100.5	23.53 ± 0.16
2011 Nov 30.96	55894.96	HST - WFC3	F160W (H band) ^{††}	1196.9	23.56 ± 0.02
2011 Nov 30.99	55894.99	HST - WFC3	F475W (SDSS g) [†]	1110.0	23.89 ± 0.02
2012 June 16.32	56094.32	VLT - FORS 2	r	400.0	24.24 ± 0.17
2012 June 16.33	56094.33	VLT - FORS 2	g	400.0	24.78 ± 0.15
2012 June 16.34	56094.34	VLT - FORS 2	u	840.0	25.14 ± 0.38
2012 June 16.35	56094.35	VLT - FORS 2	i	240.0	24.32 ± 0.17
2012 June 16.35	56094.35	VLT - FORS 2	z	720.0	23.99 ± 0.23
2012 July 18.27	56126.27	VLT - FORS2	u	840	25.39 ± 0.26
2012 July 18.26	56126.26	VLT - FORS2	g	400	24.97 ± 0.14
2012 July 18.26	56126.26	VLT - FORS2	r	400	24.48 ± 0.14
2012 July 18.28	56126.28	VLT - FORS2	i	240	24.20 ± 0.15
2012 July 18.29	56126.29	VLT - FORS2	z	720	23.81 ± 0.25
2012 Aug 22.09	56161.09	VLT - FORS2	u	840	> 25.8
2012 Aug 22.08	56161.08	VLT - FORS2	g	400	> 26.4
2012 Aug 22.08	56161.08	VLT - FORS2	r	400	> 26.0
2012 Aug 22.10	56161.10	VLT - FORS2	i	240	> 24.9
2012 Aug 22.10	56161	VLT - FORS2	z	720	> 25.2
2012 Oct 09.01	56209.01	VLT - FORS2	u	840	> 26.0
2012 Oct 09.01	56209.01	VLT - FORS2	g	400	> 26.3
2012 Oct 09.00	56209.00	VLT - FORS2	r	400	> 26.2
2012 Oct 09.02	56209.02	VLT - FORS2	i	240	> 24.8
2012 Oct 09.03	56209.03	VLT - FORS2	z	720	> 25.2
2013 Dec 10.58	56636.58	HST - WFC3	F160W (H band) ^{††}	2611.8	25.99 ± 0.08
2014 Aug 31.48	56900.48	HST/ACS - WFC	F606W	5236.0	26.78 ± 0.10

*Reported magnitudes have not been corrected for Galactic extinction ($E(B - V) = 0.095$ mag; Schlafly & Finkbeiner 2011).

Upper limits represent 3σ uncertainties. [†]HST/F475W filter has a bandpass similar to SDSS's g band. ^{††}HST/F160W filter

has a bandpass similar to the standard H band.

Table 3: Optical/Near-IR Spectra of Sw J2058+05

Date (UT)	Telescope/Instrument	Wavelength (Å)	Exposure (s)	SNR*
2011 Aug 2.41	Keck/LRIS (blue)	3360–5600	1800.0	3.4
2011 Aug 2.41	Keck/LRIS (red)	5600–10,200	1800.0	2.0
2011 Aug 4.16	VLT/FORS	3400–6100	4800.0	2.4
2011 Aug 28.47	Keck/LRIS (blue)	3360–5600	1800.0	5.3
2011 Aug 28.47	Keck/LRIS (red)	5600–10,200	1800.0	2.9
2011 Sep 2.04	VLT/XSHOOTER (UV)	3000–5560	3600.0	0.5
2011 Sep 2.04	VLT/XSHOOTER (VIS)	5300–10,200	3600.0	0.2
2011 Sep 2.04	VLT/XSHOOTER (NIR)	9900–24,800	3600.0	0.1

*Per resolution element.

Table 4: Summary of *XMM-Newton* X-ray (0.3–10 keV) Spectral Modeling of Sw J2058+05

ObsID ^a	Absorbing column ^b	Power-law index ^c	Power-law Normalization	χ^2/dof	X-ray Flux ^d
0679380801	$0.23^{+0.15}_{-0.13}$	$1.89^{+0.15}_{-0.13}$	$3.6^{+0.4}_{-0.4}$	53/48	$0.19^{+0.02}_{-0.02}$
0679380901	$0.15^{+0.18}_{-0.16}$	$1.81^{+0.18}_{-0.16}$	$2.8^{+0.4}_{-0.3}$	55/64	$0.16^{+0.02}_{-0.02}$
0694830201	$0.19^{+0.13}_{-0.12}$	$1.67^{+0.10}_{-0.10}$	$2.5^{+0.2}_{-0.2}$	86/94	$0.17^{+0.01}_{-0.01}$

^a*XMM-Newton* assigned observation ID. ^bUnits of 10^{22} atoms cm^{-2} . ^cThe X-ray spectra were modeled with *phabs*zwabs*pow* in XSPEC. The Galactic column (*phabs*) was fixed at 0.088×10^{22} atoms cm^{-2} (Kalberla et al. 2005 & Willingale et al. 2013) and the redshift in *zwabs* was fixed at 1.1853 (C12). ^dThe X-ray fluxes were estimated in the bandpass of 0.3–10 keV and have units of 10^{-12} erg s^{-1} cm^{-2} .

Table 5: Summary of UVOIR SED Modeling of Sw J2058+05^a

UTC	MJD Date (rest-frame days since discovery)	Blackbody temperature ^b	Blackbody radius ^c	χ^2/dof
2011 May 29	55710.41 (5.67)	2.9±0.5	66.6±12.4	0.3/2
2011 June 3	55715.40 (7.96)	2.9±0.5	65.4±12.9	0.3/2
2011 June 10	55722.26 (11.10)	4.9±1.1	41.3±8.1	3.8/3
2011 Aug 20	55793.07 (43.51)	2.6±0.2	70.3±8.2	12.3/3
2011 Sept 22	55826.07 (58.60)	2.6±0.2	65.2±5.4	0.2/3
2012 June 16	56094.34 (181.37)	1.5±0.2	71.3±15.5	2.5/3
2012 July 18	56126.27 (196.0)	1.4±0.1	88.1±15.0	4.7/3

^aData for the first three epochs was acquired by C12 while the rest are from Table 2.

^bUnits of 10,000 K. ^cUnits of AU (astronomical unit). The SEDs were modeled with a single-temperature blackbody.

REFERENCES

- Arcavi, I., Gal-Yam, A., Sullivan, M., et al. 2014, *ApJ*, 793, 38
- Armijo, M. M., & de Freitas Pacheco, J. A. 2013, *MNRAS*, 430, L45
- Arnaud, K. A. 1996, *Astronomical Data Analysis Software and Systems V*, 101, 17
- Appenzeller, I., Fricke, K., Fürtig, W., et al. 1998, *The Messenger*, 94, 1
- Barniol Duran, R., & Piran, T. 2013, *ApJ*, 770, 146
- Barniol Duran, R., Nakar, E., & Piran, T. 2013, *ApJ*, 772, 78
- Barthelmy, S. D., Barbier, L. M., Cummings, J. R., et al. 2005, *SSR*, 120, 143
- Berger, E., Zauderer, A., Pooley, G. G., et al. 2012, *ApJ*, 748, 36
- Bloom, J. S., Giannios, D., Metzger, B. D., et al. 2011, *Science*, 333, 203
- Bower, G. C., Metzger, B. D., Cenko, S. B., Silverman, J. M., & Bloom, J. S. 2013, *ApJ*, 763, 84
- Burrows, D. N., Hill, J. E., Nousek, J. A., et al. 2005, *Space Sci. Rev.*, 120, 165
- Burrows, D. N., Kennea, J. A., Ghisellini, G., et al. 2011, *Nature*, 476, 421
- Cenko, S. B., Bloom, J. S., Kulkarni, S. R., et al. 2012b, *MNRAS*, 420, 2684
- Cenko, S. B., Krimm, H. A., Horesh, A., et al. 2012, *ApJ*, 753, 77
- Chornock, R., Berger, E., Gezari, S., et al. 2014, *ApJ*, 780, 44
- De Colle, F., Guillochon, J., Naiman, J., & Ramirez-Ruiz, E. 2012, *ApJ*, 760, 103
- Evans, C. R., & Kochanek, C. S. 1989, *ApJ*, 346, L13
- Falcke, H., Körding, E., & Markoff, S. 2004, *A&A*, 414, 895
- Farrell, S. A., Webb, N. A., Barret, D., Godet, O., & Rodrigues, J. M. 2009, *Nature*, 460, 73
- Filippenko, A. V. 1982, *PASP*, 94, 715
- Fruchter, A. S., & Hook, R. N. 2002, *PASP*, 114, 144
- Garmire, G. P., Bautz, M. W., Ford, P. G., Nousek, J. A., & Ricker, G. R., Jr. 2003, *Proc. SPIE*, 4851, 28

- Gehrels, N., Chincarini, G., Giommi, P., et al. 2004, *ApJ*, 611, 1005
- Gezari, S., Basa, S., Martin, D. C., et al. 2008, *ApJ*, 676, 944
- Gezari, S., Chornock, R., Rest, A., et al. 2012, *Nature*, 485, 217
- Gezari, S., Heckman, T., Cenko, S. B., et al. 2009, *ApJ*, 698, 1367
- Granot, J., & Sari, R. 2002, *ApJ*, 568, 820
- Giannios, D., & Metzger, B. D. 2011, *MNRAS*, 416, 2102
- Greisen, E. W. 2003, *Information Handling in Astronomy - Historical Vistas*, 285, 109
- Guillochon, J., Manukian, H., & Ramirez-Ruiz, E. 2014, *ApJ*, 783, 23
- Hills, J. G. 1975, *Nature*, 254, 295
- Hook, I. M., Jørgensen, I., Allington-Smith, J. R., et al. 2004, *PASP*, 116, 425
- Holoien, T. W.-S., Prieto, J. L., Bersier, D., et al. 2014, *MNRAS*, 445, 3263
- Jansen, F., Lumb, D., Altieri, B., et al. 2001, *A&A*, 365, L1
- Kaaret, P., Feng, H., & Gorski, M. 2009, *ApJ*, 692, 653
- Kalberla, P. M. W., Burton, W. B., Hartmann, D., et al. 2005, *A&A*, 440, 775
- Kennicutt, R. C., Jr. 1998, *ApJ*, 498, 541
- Krimm, H. A., Kennea, J. A., Holland, S. T., et al. 2011, *The Astronomer's Telegram*, 3384, 1
- Krolik, J. H., & Piran, T. 2011, *ApJ*, 743, 134
- Kulkarni, S. R., Frail, D. A., Wieringa, M. H., et al. 1998, *Nature*, 395, 663
- Lauer, T. R., Faber, S. M., Richstone, D., et al. 2007, *ApJ*, 662, 808
- Leahy, D. A., Darbro, W., Elsner, R. F., et al. 1983, *ApJ*, 266, 160
- Levan, A. J., & Tanvir, N. R. 2012, *The Astronomer's Telegram*, 4610, 1
- Levan, A. J., Tanvir, N. R., Cenko, S. B., et al. 2011, *Science*, 333, 199
- Lodato, G., & Rossi, E. M. 2011, *MNRAS*, 410, 359

- Merloni, A., Heinz, S., & di Matteo, T. 2003, *MNRAS*, 345, 1057
- Metzger, B. D., Giannios, D., & Mimica, P. 2012, *MNRAS*, 420, 3528
- Miller, M. C., & Colbert, E. J. M. 2004, *International Journal of Modern Physics D*, 13, 1
- Ohsuga, K., Mori, M., Nakamoto, T., & Mineshige, S. 2005, *ApJ*, 628, 368
- Oke, J. B., Cohen, J. G., Carr, M., et al. 1995, *PASP*, 107, 375
- Pasham, D. R., Strohmayer, T. E., & Mushotzky, R. F. 2014, *Nature*, 513, 74
- Pei, Y. C. 1992, *ApJ*, 395, 130
- Pirard, J.-F., Kissler-Patig, M., Moorwood, A., et al. 2004, *Proc. SPIE*, 5492, 1763
- Plotkin, R. M., Markoff, S., Kelly, B. C., Körding, E., & Anderson, S. F. 2012, *MNRAS*, 419, 267
- Readhead, A. C. S. 1994, *ApJ*, 426, 51
- Rees, M. J. 1988, *Nature*, 333, 523
- Saxton, R. D., Read, A. M., Esquej, P., et al. 2012, *A&A*, 541, AA106
- Saxton, C. J., Soria, R., Wu, K., & Kuin, N. P. M. 2012, *MNRAS*, 422, 1625
- Sbarufatti, B., Burrows, D. N., Gehrels, N., & Kennea, J. A. 2012, *The Astronomer’s Telegram*, 4398, 1
- Schlaafy, E. F., & Finkbeiner, D. P. 2011, *ApJ*, 737, 103
- Spergel, D. N., Bean, R., Doré, O., et al. 2007, *ApJS*, 170, 377
- Strubbe, L. E., & Quataert, E. 2009, *MNRAS*, 400, 2070
- Strüder, L., Briel, U., Dennerl, K., et al. 2001, *A&A*, 365, L18
- Tchekhovskoy, A., Metzger, B. D., Giannios, D., & Kelley, L. Z. 2014, *MNRAS*, 437, 2744
- Tchekhovskoy, A., Narayan, R., & McKinney, J. C. 2010, *ApJ*, 711, 50
- Turner, M. J. L., Abbey, A., Arnaud, M., et al. 2001, *A&A*, 365, L27
- Vanden Berk, D. E., Richards, G. T., Bauer, A., et al. 2001, *AJ*, 122, 549
- van Velzen, S., Frail, D. A., Körding, E., & Falcke, H. 2013, *A&A*, 552, AA5

- Vernet, J., Dekker, H., D’Odorico, S., et al. 2011, *A&A*, 536, AA105
- Webb, N., Cseh, D., Lenc, E., et al. 2012, *Science*, 337, 554
- Weisskopf, M. C., Brinkman, B., Canizares, C., et al. 2002, *PASP*, 114, 1
- Wiersema, K., van der Horst, A. J., Levan, A. J., et al. 2012, *MNRAS*, 421, 1942
- Willingale, R., Starling, R. L. C., Beardmore, A. P., Tanvir, N. R., & O’Brien, P. T. 2013, *MNRAS*, 431, 394
- Zauderer, B. A., Berger, E., Margutti, R., et al. 2013, *ApJ*, 767, 152
- Zauderer, B. A., Berger, E., Soderberg, A. M., et al. 2011, *Nature*, 476, 425